

Bipolarized Weyl semimetals and quantum crystal valley Hall effect in two-dimensional altermagnetic materials

Chao-Yang Tan^{1,2}, Ze-Feng Gao^{1,2}, Huan-Cheng Yang^{1,2}, Kai Liu^{1,2}, Peng-Jie Guo^{1,2,*} and Zhong-Yi Lu^{1,2,3†}

1. Department of Physics and Beijing Key Laboratory of Opto-electronic Functional Materials & Micro-nano Devices. Renmin University of China, Beijing 100872, China

2. Key Laboratory of Quantum State Construction and Manipulation (Ministry of Education), Renmin University of China, Beijing 100872, China and

3. Hefei National Laboratory, Hefei 230088, China

(Dated: June 25, 2024)

Magnetism and topology are two major areas of condensed matter physics. The combination of magnetism and topology gives rise to more novel physical effects, which have attracted strongly theoretical and experimental attention. Recently, the concept of altermagnetism has been introduced, characterized by a dual nature: real-space antiferromagnetism and reciprocal-space anisotropic spin polarization. The amalgamation of altermagnetism with topology may lead to the emergence of previously unobserved topological phases and the associated physical effects. In this study, utilizing a four-band lattice model that incorporates altermagnetism and spin group symmetry, we demonstrate that type-I, type-II, and type-III bipolarized Weyl semimetals can exist in altermagnetic systems. Through the first-principles electronic structure calculations, we predict four ideal two-dimensional type-I altermagnetic bipolarized Weyl semimetals Fe_2WTe_4 and Fe_2MoZ_4 ($Z=\text{S,Se,Te}$). More significantly, we introduce the quantum crystal valley Hall effect, a phenomenon achievable in three of these materials namely Fe_2WTe_4 , Fe_2MoS_4 , and Fe_2MoTe_4 , when spin-orbit coupling is considered. Furthermore, these materials have the potential to transition from a quantum crystal valley Hall phase to a Chern insulator phase under strain. In contrast, Fe_2MoSe_4 remains to be a Weyl semimetal under spin-orbit coupling but is distinguished by possessing only a single pair of Weyl points. Additionally, the position, polarization, and number of Weyl points in Fe_2WTe_4 and Fe_2MoZ_4 can be manipulated by adjusting the direction of the Néel vector. Consequently, Fe_2WTe_4 and Fe_2MoZ_4 emerge as promising experimental platforms for investigating the distinctive physical attributes of various altermagnetic topological phases.

Introduction. The topological Weyl semimetals have attracted much attention due to their novel physical properties, such as topological protected Fermi arc, chiral zero sound, chiral anomaly, large magnetoresistance effect, large intrinsic anomalous Hall effect [1–13], etc. Since Weyl points are formed by linear crossing of two nondegenerate energy bands, Weyl semimetals can only exist in the materials without the joint symmetry of time reversal and space inversion. The Weyl points of nonmagnetic or conventional antiferromagnetic Weyl semimetals have no spin polarization (Fig. 1(a)), while the Weyl points of ferromagnetic Weyl semimetals have only spin-up or spin-down polarization (Fig. 1(b)). This then raises an intriguing question: Can a Weyl semimetal accommodate both spin-up and spin-down polarized Weyl points simultaneously?(Fig. 1(c)).

Recently, based on spin group theory, a new magnetic phase, namely altermagnetism, which is different from ferromagnetism and conventional antiferromagnetism, has been proposed [14–20]. Due to the duality of real-space antiferromagnetism and reciprocal-space anisotropic spin polarization similar to ferromagnetism, the altermagnetic materials show many novel physical effects, including spin-splitting torque [21–24], giant magnetoresistance (GMR) effect [25], tunneling magnetore-

sistance (TMR) effect [25, 26], piezomagnetic effect [27], nontrivial superconductivity [28, 29], time-reversal odd anomalous effect [15, 30–35], quantum anomalous Hall effect [36], higher-order topological states [37], altermagnetic ferroelectricity [38], strong spin-orbit coupling effect in light element altermagnetic materials [39] and so on. Moreover, the already predicted altermagnetic materials cover metals, semimetals, and insulators, which provides a guarantee for the realization of many novel physical effects in experiments [40–47]. Meanwhile, the reciprocal-space anisotropic spin polarization of altermagnetism also provides possibility to realize a topological Weyl semimetal with both spin-up and spin-down polarized Weyl points. Here, we term this class of Weyl semimetals as bipolarized Weyl semimetals.

In this work, based on spin group symmetry analysis, lattice model, and the first-principles electronic structure calculations, we not only demonstrate that type-I, type-II, and type-III bipolarized Weyl semimetal can be realized in altermagnetic systems, but also predict four ideal two-dimensional type-I bipolarized Weyl semimetals Fe_2WTe_4 and Fe_2MoZ_4 ($Z=\text{S,Se,Te}$). Furthermore, we find quantum crystal valley Hall effect in Fe_2WTe_4 , Fe_2MoS_4 , and Fe_2MoSe_4 . And they can transform from quantum crystal valley Hall phase to Chern insulator phase under strain. In contrast, Fe_2MoTe_4 remains to be a Weyl semimetal with only one pair of Weyl points under spin-orbit coupling (SOC).

Lattice Model. We consider a square lattice containing

* guopengjie@ruc.edu.cn

† zlu@ruc.edu.cn

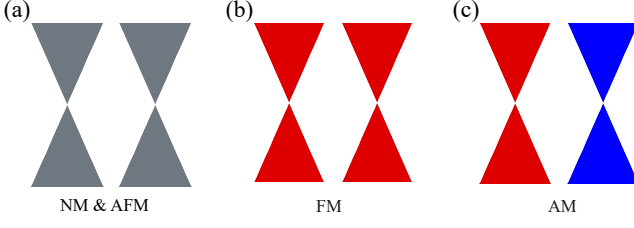


FIG. 1. The schematic diagrams of three different Weyl semimetal phases. (a) Nonmagnetic (NM) or antiferromagnetic (AFM) Weyl semimetal; (b) Ferromagnetic (FM) semimetal; (c) bipolarized altermagnetic (AM) semimetal. The gray cones represent Weyl points without spin polarization. The red and blue cones represent spin-up and spin-down polarized Weyl points, respectively.

two sites (labeled by sublattice index $\alpha = 1, 2$) within a unit cell (Fig. 2(a)). The corresponding tight-binding (TB) model is

$$\begin{aligned}
 H = & \sum_{d_i, j} \left[t^d C_{1, j}^\dagger C_{2, j+d_i} + h.c. \right] \\
 & + \sum_{\alpha, j} \left[t_\alpha^x C_{\alpha, j}^\dagger C_{\alpha, j+\mathbf{x}} + t_\alpha^y C_{\alpha, j}^\dagger C_{\alpha, j+\mathbf{y}} + h.c. \right] \\
 & + \sum_{\alpha, j} \mathbf{m}_\alpha \cdot \boldsymbol{\sigma} C_{\alpha, j}^\dagger C_{\alpha, j}
 \end{aligned} \quad (1)$$

where $C_{\alpha, j}^\dagger = (C_{\alpha, j\uparrow}^\dagger, C_{\alpha, j\downarrow}^\dagger)$ and $C_{\alpha, j} = (C_{\alpha, j\uparrow}, C_{\alpha, j\downarrow})$ represent electron creation and annihilation operators, respectively. The terms containing t^d and $t_\alpha^{x, y}$ represent the nearest and next nearest hopping, respectively. As illustrated in Fig. 2(a), $\mathbf{d}_{1,4} = \pm \frac{1}{2}(\mathbf{x} + \mathbf{y})$, $\mathbf{d}_{2,3} = \pm \frac{1}{2}(\mathbf{x} - \mathbf{y})$ and $\mathbf{x} = a_1 \hat{x}$, $\mathbf{y} = a_2 \hat{y}$ denote the direction of hopping, where a_1, a_2 are the lattice constants along the unit vectors \hat{x}, \hat{y} . The σ_0 and $\boldsymbol{\sigma}$ are identity matrix and Pauli matrix, respectively. The $\mathbf{m}_1 = -\mathbf{m}_2 = \mathbf{m}$ stands for the static collinear AFM order, which couples to the electron spin as a Zeeman field. Due to the two opposite spin sites located at the space-inversion invariant position, the collinear AFM order breaks spin symmetry $\{C_2^\perp || I\}$. Moreover, since $t_1^{x, y} \neq t_2^{x, y}$ breaks the spin symmetry $\{C_2^\perp || \tau\}$ but $t_1^{x, y} = t_2^{y, x}$ preserves spin symmetry $\{C_2^\perp || C_{4z}\}$. Thus, this lattice model is a d -wave altermagnetism.

After performing the Fourier transformation, the TB Hamiltonian can be rewritten as $H = \sum_k \psi_k^\dagger H_0 \psi_k$ in momentum space with basis $\psi_k^\dagger = (C_{1k\uparrow}^\dagger, C_{1k\downarrow}^\dagger, C_{2k\uparrow}^\dagger, C_{2k\downarrow}^\dagger)$, where H_0 reads

$$H_0 = \Gamma_k^+ \tau_0 \sigma_0 + \Gamma_k^{12} \tau_x \sigma_0 + \Gamma_k^- \tau_z \sigma_0 + \tau_z \mathbf{m} \cdot \boldsymbol{\sigma} \quad (2)$$

in which Pauli matrix $\boldsymbol{\tau}$ is the pseudospin matrix in lattice space. The auxiliary functions $\Gamma_k^{12} = 4t^d \cos \frac{k_x}{2} \cos \frac{k_y}{2}$ and $\Gamma_k^\pm = (t_1 \pm t_2) \cos k_x + (t_2 \pm t_1) \cos k_y$ with $t_\alpha^x = t_\alpha$ are related to inter- and intra-sublattice hoppings, respectively. Altermagnetism leads to anisotropic

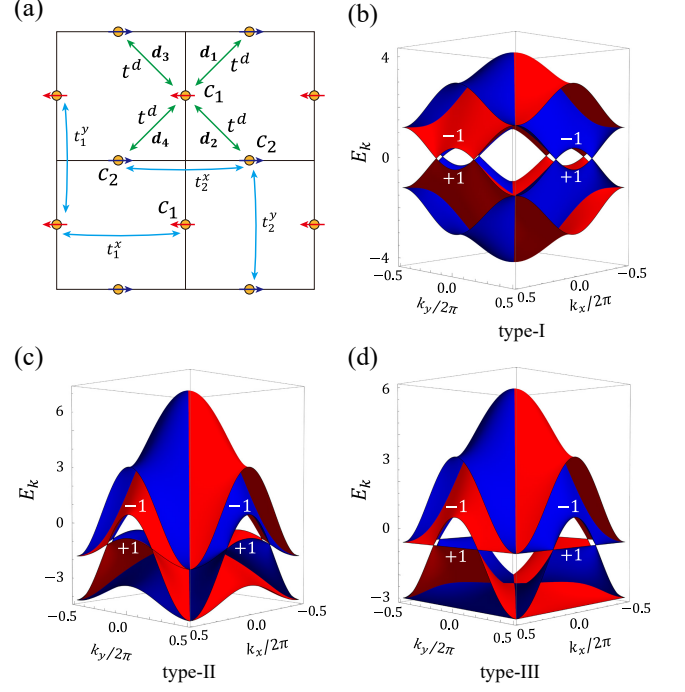


FIG. 2. Two-dimensional lattice model with altermagnetism. (a) The schematic illustration for the hoppings between lattice sites for the Hamiltonian Eq. (1). The red and blue arrows represent spin-up and spin-down magnetic moments, respectively. (b-d) The band structure of lattice model in certain parameters. (b), type-I bipolarized Weyl semimetal; (c), type-II bipolarized Weyl semimetal; (d), type-III bipolarized Weyl semimetal. The red and blue represent spin-up and spin-down bands, respectively. The 1 and -1 represent eigenvalues of the spin symmetry $\{E || C_{2x}\}$ or $\{E || C_{2y}\}$.

spin splitting, so what does the size of spin splitting depend on? The lattice model analysis shows the size of spin splitting is determined by the strength of anisotropic hopping $|t_1 - t_2|$ (Detailed calculations and analyses are presented in the supplementary materials (SM)).

When $2|t_1 - t_2| > |\mathbf{m}|$, the band crossing occurs, which is a necessary condition for the realization of bipolarized Weyl semimetals. Further symmetry analysis shows that there are two crossing points with spin-up polarization and another two crossing points with spin-down polarization protected by the spin symmetry $\{E || C_{2y}\}$ and $\{E || C_{2x}\}$, respectively. Therefore, a bipolarized Weyl semimetal can be realized in an altermagnetic system. Interestingly, by adjusting the hopping terms t_1 and t_2 , we are able to achieve type-I, type-II, and type-III bipolarized Weyl semimetals which are shown in Fig. 2(b), (c), and (d), respectively.

Candidate materials. Monolayer Fe_2XZ_4 (Fe_2WTe_4 and Fe_2MoZ_4) takes a square lattice structure with the symmorphic space group $P-42m$ (No.111) symmetry and the corresponding point group is D_{2d} with generators S_{4z} and C_{2x} . Monolayer Fe_2XZ_4 contains three atomic layers where Fe_2X atomic layer is sandwiched by two Z atomic

layers as shown in Fig. 3(a) and (b), and the corresponding BZ is shown in Fig. 3(c). Moreover, the dynamical stability of monolayer Fe_2XZ_4 is confirmed by the phonon calculations (Fig. S3) [48]. Since the crystal structure of monolayer Fe_2XZ_4 is proposed based on the already synthesized layered Cu_2XZ_4 ($\text{Z}=\text{S,Se}$) [49–53] and Ag_2WS_4 [54], monolayer Fe_2XZ_4 may be synthesized experimentally in a similar way.

To determine the magnetic ground states of monolayer Fe_2XZ_4 , we consider three likely magnetic structures including one ferromagnetic and two antiferromagnetic ones (Fig. S4). The calculated results show that the AFM1 is always magnetic ground state for the four materials Fe_2XZ_4 , as shown in Table. S2. From Fig. 3(a), the magnetic and crystal primitive cells are identical, thus Fe_2XZ_4 has no $\{C_2^\perp|\tau\}$ spin symmetry. And due to the lack of space-inversion symmetry, Fe_2XZ_4 must not have $\{C_2^\perp|I\}$ spin symmetry. Meanwhile, the Fe_2XZ_4 has $\{C_2^\perp|S_{4z}\}$ spin symmetry. Thus, all the Fe_2XZ_4 are d -wave altermagnetic materials. In the following, we present nontrivial topological states with Fe_2WTe_4 as a representative material, while the calculated results of other three materials are presented in the SM.

For monolayer Fe_2WTe_4 , the W atom is at the corner of primitive cell and there is no W atom in the center, which leads to a strongly anisotropic polarized charge density around the magnetic Fe atom as shown in Fig. 3(d). The strongly anisotropic polarized charge density makes x - or y -directional two hopping interactions of the next nearest Fe atoms very different, which can lead to the large spin splitting in the non-relativistic case according to our lattice model analysis. Just like our analysis, the spin splitting caused by the exchange interactions in altermagnetic Fe_2WTe_4 is very large. The spins of these bands along the Γ -X and Γ -Y are opposite, reflecting the characteristics of d -wave altermagnetism (Fig. 3(e)). More significantly, altermagnetic Fe_2WTe_4 is a perfect semimetal with only four doubly degenerate crossing points at the Fermi level (Fig. 3(c) and (e)). These crossing points can be considered as a valley degree of freedom, similar to the case of graphene. Manipulating this valley degree of freedom will give rise to novel effects as shown below. The further orbital weight analysis shows that the two crossing bands along the Γ -Y direction are respectively contributed by the e_g and d_{yz} orbitals of Fe atoms (Fig. 3(f)). Since the e_g orbital is invariable but the d_{yz} orbital changes to $-d_{yz}$ under the $\{E|C_{2y}\}$ operation, the corresponding eigenvalues of the two crossing bands are 1 and -1 , respectively. Thus, the two crossing points on the Γ -Y direction are the Weyl points protected by $\{E|C_{2y}\}$ spin symmetry. Likewise, the two crossing points on the Γ -X direction are also the Weyl points protected by $\{E|C_{2x}\}$ spin symmetry. Interestingly, the two Weyl points on the Γ -Y direction have spin-up polarization, while the two Weyl points in the Γ -X direction have spin-down polarization (Fig. 3(e)). Thus, the monolayer altermagnetic Fe_2WTe_4 is a bipolarized Weyl semimetal.

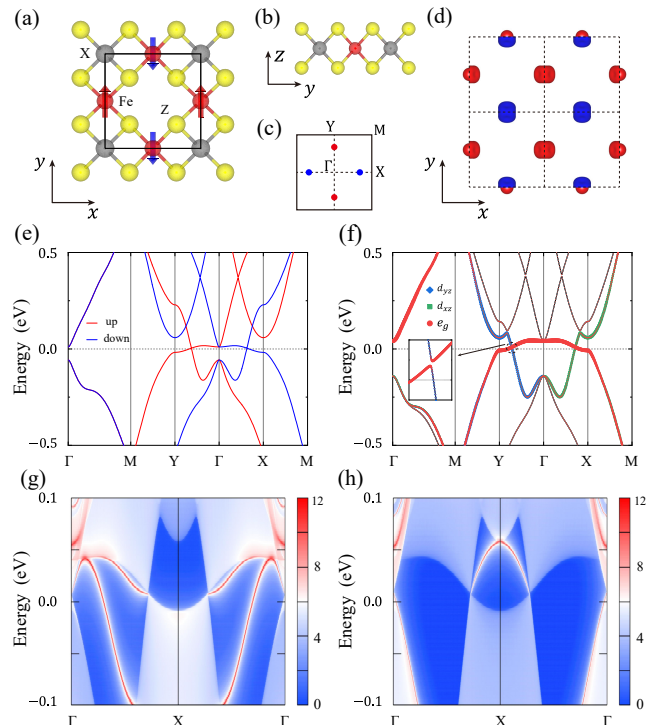


FIG. 3. Crystal and magnetic structures of monolayer Fe_2XZ_4 and electronic properties of monolayer Fe_2WTe_4 . (a) and (b) represent the top and side views of crystal and magnetic structure of Fe_2XZ_4 , respectively. The red and blue arrows represent spin-up and spin-down magnetic moments, respectively. (c) The Brillouin zone (BZ) of Fe_2XZ_4 where the high-symmetry points are labeled. The red and blue points represent spin-up and spin-down polarized Weyl points, respectively. (d) The polarization charge density of Fe_2WTe_4 without SOC (red: spin-up, blue: spin-down). The electronic structure along the high-symmetry directions without SOC (e) and with SOC (f). The e_g represents the d_{z^2} and $d_{x^2-y^2}$ orbitals of Fe element. The Spectral function of monolayer Fe_2WTe_4 with a semi-infinite termination left (g) and right (h) edges.

With SOC, monolayer Fe_2WTe_4 changes from spin group symmetry to magnetic group symmetry. According to our magnetic anisotropy calculations, the direction of the Néel vector is along the z -axis, which has magnetic point group symmetry $2S_{4z}T$, C_{2z} , $C_{2x}T$, $C_{2y}T$, and $2\sigma_d$. The symmetry of Γ -Y axis changes from the $\{E|C_{2y}\}$ spin symmetry to the $C_{2x}T$ symmetry. Both e_g and d_{yz} orbitals are invariant under the C_{2x} operation, so the two crossing bands in the Γ -Y direction have the same irreducible representation, thus opening a gap (2.5 meV) (inset of Fig. 3(f)). Likewise, the two Weyl points in the Γ -X direction also open a gap of 2.5 meV. Due to the C_{2z} symmetry, the two Weyl points in the Γ -X or Γ -Y direction contribute the same Berry curvature, but the two pairs of Weyl points in the Γ -X and Γ -Y directions contribute the opposite Berry curvature due to the $S_{4z}T$ symmetry (Fig. 4(a)). We know that a two-dimensional linear Weyl point has π Berry curvature, so

one pair of Weyl points in the Γ -X (Γ -Y) direction contributes -2π (2π) Berry curvature, which corresponds to the Chern number -1 (1). Furthermore, the anisotropy Chern number may lead to nontrivial chiral edge states, which have been confirmed by the calculations of edge states (Fig. 3(g) and (h)). On the other hand, under the strain in the x direction, the band inversion of Fe_2WTe_4 in the Γ -X direction disappears, but the band inversion in the Γ -Y direction still remains (Fig. S9). Thus, monolayer altermagnetic Fe_2WTe_4 transforms into a Chern insulator with quantum anomalous Hall effect under strain.

Quantum crystal valley Hall effect. As is well known, under in-plane longitudinal electric field, an intrinsic Berry curvature can induce an anomalous Hall velocity for the Bloch electrons in two-dimensional materials ($v \sim E \times \Omega(k)$) [55]. For monolayer Fe_2WTe_4 , there are four valleys originating from the Weyl points (Fig. 4(a)). From Fig. 4(a), the valley electrons in the Γ -X and Γ -Y directions for Fe_2WTe_4 have opposite Berry curvature, resulting in opposite anomalous Hall velocities under the in-plane longitudinal electric field (Fig. 4(b)). Moreover, these valley electrons maintain opposite spin polarization under SOC (Fig. 4(a)), thus altermagnetic Fe_2WTe_4 can generate polarized spin currents perpendicular to the electric field, akin to the valley Hall effect in monolayer MoS_2 [56, 57]. For monolayer MoS_2 , the time-reversal symmetry guarantees opposite Berry curvature and angular momentum for the valley electrons with opposite momentum, which results in the valley Hall effect. In comparison, Fe_2WTe_4 breaks the time-reversal symmetry, but the $S_{4z}T$ symmetry ensures opposite Berry curvature and spin polarization for the valley electrons in both Γ -X and Γ -Y directions. Due to the valley Hall effect deriving from crystal symmetry, the valley Hall effect in monolayer altermagnetic Fe_2WTe_4 can be called crystal valley Hall effect. More importantly, the two pairs of valley electrons in the Γ -X and Γ -Y directions contribute opposite Chern numbers, thus the valley Hall effect in monolayer altermagnetic Fe_2WTe_4 can be further called quantum crystal valley Hall effect, which is similar to the quantum valley Hall effect in two-dimensional nonmagnetic materials [12, 58].

On the other hand, our calculations show that the other three two-dimensional altermagnetic materials are also bipolarized Weyl semimetals without SOC. The directions of the Néel vector of both Fe_2MoS_4 and Fe_2MoSe_4 are the same as that of Fe_2WTe_4 under SOC, so the quantum crystal valley Hall effect can also be realized in both Fe_2MoS_4 and Fe_2MoSe_4 (Fig. S6 and S7). Meanwhile, both Fe_2MoS_4 and Fe_2MoSe_4 also transform from quantum crystal valley Hall insulator phase to Chern insulator phase under strain (Fig. S9).

Different from the case of Fe_2MoS_4 , Fe_2MoSe_4 and Fe_2WTe_4 , the direction of Néel vector of Fe_2MoTe_4 is along the x - or y -axis due to the S_4 symmetry of crystal. When the Néel vector is along the x -axis, because there is no any symmetry for the Γ -Y axis, the pair of spin-up polarized Weyl points in Fe_2MoTe_4 open gap, while

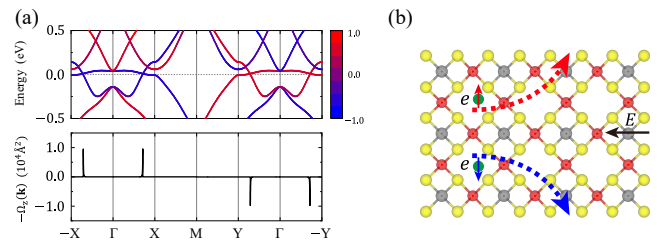


FIG. 4. (a) Top panel: the electronic band structure of monolayer Fe_2WTe_4 with the spin projection s_z ; bottom panel: the corresponding berry curvature along the high-symmetry line. (b) The schematic diagram of the topological valley Hall effect in monolayer Fe_2WTe_4 . The E and e represent external electric field and electrons, respectively. The red and blue arrows represent up and down spins, respectively.

the two spin-down polarized Weyl points in the Γ -X axis remain stable protected by the C_{2x} symmetry. Therefore, monolayer altermagnetic Fe_2MoTe_4 is still a Weyl semimetal under SOC (Fig. S5(f)). Similarly, Fe_2MoTe_4 has also only one pair of Weyl points, but the pair of Weyl points have spin-up polarization when the Néel vector is along the y -axis. If the Néel vector is along the xy direction, the Γ -X and Γ -Y axes do not have any symmetry, thus the two pairs of Weyl points of Fe_2MoTe_4 open gap (Fig. S8). However, the $C_{2z}T$ symmetry is always present for the Néel vector in the xy plane, which results in the Berry curvature $\Omega_z(k)$ to be zero in the whole BZ, thus the quantum crystal valley Hall effect can not be realized in Fe_2MoTe_4 . According to the above analysis, the position, polarization, and number of Weyl points of Fe_2MoTe_4 , as well as Fe_2MoS_4 , Fe_2MoSe_4 and Fe_2WTe_4 (Fig. S8), can be manipulated by controlling the Néel vector.

In conclusion, our research, grounded in symmetry analysis, lattice modeling, and first-principles electronic structure calculations, not only confirms the theoretical feasibility of realizing a bipolarized Weyl semimetal in two-dimensional altermagnetic systems but also identifies four ideal candidates: Fe_2WTe_4 and Fe_2MoZ_4 ($Z=\text{S,Se,Te}$). Most notably, we propose that the quantum crystal valley Hall effect can be induced in the monolayer altermagnetic materials Fe_2WTe_4 , Fe_2MoS_4 , and Fe_2MoSe_4 when subject to spin-orbit coupling. These materials can further transition from a quantum crystal valley Hall insulator phase to a Chern insulator phase under strain. Unlike the other materials mentioned, Fe_2MoTe_4 retains its Weyl semimetal nature with a single pair of Weyl points even under SOC. Furthermore, the position, polarization, and number of Weyl points in Fe_2WTe_4 and Fe_2MoZ_4 ($Z=\text{S,Se,Te}$) can be manipulated by adjusting the direction of the Néel vector. Consequently, Fe_2WTe_4 and Fe_2MoZ_4 offer a promising experimental platform for exploring the distinctive physical properties associated with multiple altermagnetic topological phases.

ACKNOWLEDGMENTS

This work was financially supported by the National Natural Science Foundation of China (Grant No.11934020, No.12204533, No.62206299 and No.12174443), the Beijing Natural Science Foundation

(Grant No.Z200005) and the Innovation Program for Quantum Science and Technology (2021ZD0302402). Computational resources have been provided by the Physical Laboratory of High Performance Computing at Renmin University of China.

-
- [1] X. Wan, A. M. Turner, A. Vishwanath, and S. Y. Savrasov, Topological semimetal and Fermi-arc surface states in the electronic structure of pyrochlore iridates, *Phys. Rev. B* **83**, 205101 (2011).
- [2] G. Xu, H. Weng, Z. Wang, X. Dai, and Z. Fang, Chern Semimetal and the Quantized Anomalous Hall Effect in HgCr_2Se_4 , *Phys. Rev. Lett.* **107**, 186806 (2011).
- [3] H. Weng, C. Fang, Z. Fang, B. A. Bernevig, and X. Dai, Weyl Semimetal Phase in Noncentrosymmetric Transition-Metal Monophosphides, *Phys. Rev. X* **5**, 011029 (2015).
- [4] H. Weng, X. Dai, and Z. Fang, Topological semimetals predicted from first-principles calculations, *J. Phys.: Condens. Matter* **28**, 303001 (2016).
- [5] S.-Y. Xu, I. Belopolski, N. Alidoust, M. Neupane, G. Bian, C. Zhang, R. Sankar, G. Chang, Z. Yuan, C.-C. Lee, S.-M. Huang, H. Zheng, J. Ma, D. S. Sanchez, B. Wang, A. Bansil, F. Chou, P. P. Shibayev, H. Lin, S. Jia, and M. Z. Hasan, Discovery of a Weyl fermion semimetal and topological Fermi arcs, *Science* **349**, 613 (2015).
- [6] X. Huang, L. Zhao, Y. Long, P. Wang, D. Chen, Z. Yang, H. Liang, M. Xue, H. Weng, Z. Fang, X. Dai, and G. Chen, Observation of the Chiral-Anomaly-Induced Negative Magnetoresistance in 3D Weyl Semimetal TaAs, *Phys. Rev. X* **5**, 031023 (2015).
- [7] Q. Wang, Y. Xu, R. Lou, Z. Liu, M. Li, Y. Huang, D. Shen, H. Weng, S. Wang, and H. Lei, Large intrinsic anomalous Hall effect in half-metallic ferromagnet $\text{Co}_3\text{Sn}_2\text{S}_2$ with magnetic Weyl fermions, *Nat. Commun.* **9**, 3681 (2018).
- [8] E. Liu, Y. Sun, N. Kumar, L. Muechler, A. Sun, L. Jiao, S.-Y. Yang, D. Liu, A. Liang, Q. Xu, J. Kroder, V. Süß, H. Borrmann, C. Shekhar, Z. Wang, C. Xi, W. Wang, W. Schnelle, S. Wirth, Y. Chen, S. T. B. Goennenwein, and C. Felser, Giant anomalous Hall effect in a ferromagnetic kagome-lattice semimetal, *Nat. Phys.* **14**, 1125 (2018).
- [9] Z. Song and X. Dai, Hear the Sound of Weyl Fermions, *Phys. Rev. X* **9**, 021053 (2019).
- [10] J. Xiang, S. Hu, Z. Song, M. Lv, J. Zhang, L. Zhao, W. Li, Z. Chen, S. Zhang, J.-T. Wang, Y.-f. Yang, X. Dai, F. Steglich, G. Chen, and P. Sun, Giant Magnetic Quantum Oscillations in the Thermal Conductivity of TaAs: Indications of Chiral Zero Sound, *Phys. Rev. X* **9**, 031036 (2019).
- [11] X. Zhao, P.-J. Guo, F. Ma, and Z.-Y. Lu, Coexistence of topological Weyl and nodal-ring states in ferromagnetic and ferrimagnetic double perovskites, *Phys. Rev. B* **103**, 085138 (2021).
- [12] X. Zhao, F. Ma, P.-J. Guo, and Z.-Y. Lu, Two-dimensional quadratic double Weyl semimetal, *Phys. Rev. Res.* **4**, 043183 (2022).
- [13] Q. Liu, Y. Fu, P. Ding, H. Ma, P. Guo, H. Lei, and S. Wang, Coexistence of Dirac and Weyl points in non-centrosymmetric semimetal NbIrTe_4 , *Chin. Phys. B* **33**, 047104 (2024).
- [14] S. Hayami, Y. Yanagi, and H. Kusunose, Momentum-Dependent Spin Splitting by Collinear Antiferromagnetic Ordering, *J. Phys. Soc. Jpn.* **88**, 123702 (2019).
- [15] L. Šmejkal, R. González-Hernández, T. Jungwirth, and J. Sinova, Crystal time-reversal symmetry breaking and spontaneous Hall effect in collinear antiferromagnets, *Sci. Adv.* **6**, eaaz8809 (2020).
- [16] L.-D. Yuan, Z. Wang, J.-W. Luo, E. I. Rashba, and A. Zunger, Giant momentum-dependent spin splitting in centrosymmetric low- Z antiferromagnets, *Phys. Rev. B* **102**, 014422 (2020).
- [17] I. I. Mazin, K. Koepernik, M. D. Johannes, R. González-Hernández, and L. Šmejkal, Prediction of unconventional magnetism in doped FeSb_2 , *Proc. Natl. Acad. Sci. U.S.A.* **118**, e2108924118 (2021).
- [18] L. Šmejkal, J. Sinova, and T. Jungwirth, Emerging Research Landscape of Altermagnetism, *Phys. Rev. X* **12**, 040501 (2022).
- [19] L. Šmejkal, J. Sinova, and T. Jungwirth, Beyond Conventional Ferromagnetism and Antiferromagnetism: A Phase with Nonrelativistic Spin and Crystal Rotation Symmetry, *Phys. Rev. X* **12**, 031042 (2022).
- [20] I. Mazin, Editorial: Altermagnetism—a new punch line of fundamental magnetism, *Phys. Rev. X* **12**, 040002 (2022).
- [21] R. González-Hernández, L. Šmejkal, K. Výborný, Y. Yahagi, J. Sinova, T. c. v. Jungwirth, and J. Železný, Efficient Electrical Spin Splitter Based on Nonrelativistic Collinear Antiferromagnetism, *Phys. Rev. Lett.* **126**, 127701 (2021).
- [22] A. Bose, N. J. Schreiber, R. Jain, D.-F. Shao, H. P. Nair, J. Sun, X. S. Zhang, D. A. Muller, E. Y. Tsybal, D. G. Schlom, and D. C. Ralph, Tilted spin current generated by the collinear antiferromagnet ruthenium dioxide, *Nat. Electron.* **5**, 267 (2022).
- [23] H. Bai, L. Han, X. Y. Feng, Y. J. Zhou, R. X. Su, Q. Wang, L. Y. Liao, W. X. Zhu, X. Z. Chen, F. Pan, X. L. Fan, and C. Song, Observation of Spin Splitting Torque in a Collinear Antiferromagnet RuO_2 , *Phys. Rev. Lett.* **128**, 197202 (2022).
- [24] S. Karube, T. Tanaka, D. Sugawara, N. Kadoguchi, M. Kohda, and J. Nitta, Observation of Spin-Splitter Torque in Collinear Antiferromagnetic RuO_2 , *Phys. Rev. Lett.* **129**, 137201 (2022).
- [25] L. Šmejkal, A. B. Hellenes, R. González-Hernández, J. Sinova, and T. Jungwirth, Giant and Tunneling Magnetoresistance in Unconventional Collinear Antiferromagnets with Nonrelativistic Spin-Momentum Coupling, *Phys. Rev. X* **12**, 011028 (2022).

- [26] D.-F. Shao, S.-H. Zhang, M. Li, C.-B. Eom, and E. Tsymbal, Spin-neutral currents for spintronics, *Nat. Commun.* **12**, 7061 (2021).
- [27] H.-Y. Ma, M. Hu, N. Li, J. Liu, W. Yao, J.-F. Jia, and J. Liu, Multifunctional antiferromagnetic materials with giant piezomagnetism and noncollinear spin current, *Nat. Commun.* **12**, 2846 (2021).
- [28] D. Zhu, Z.-Y. Zhuang, Z. Wu, and Z. Yan, Topological superconductivity in two-dimensional altermagnetic metals, *Phys. Rev. B* **108**, 184505 (2023).
- [29] Y.-X. Li and C.-C. Liu, Majorana corner modes and tunable patterns in an altermagnet heterostructure, *Phys. Rev. B* **108**, 205410 (2023).
- [30] L. Šmejkal, A. H. MacDonald, J. Sinova, S. Nakatsuji, and T. Jungwirth, Anomalous Hall antiferromagnets, *Nat. Rev. Mater.* **7**, 482 (2022).
- [31] Z. Feng, X. Zhou, L. Šmejkal, L. Wu, Z. Zhu, H. Guo, R. González-Hernández, X. Wang, H. Yan, P. Qin, X. Zhang, H. Wu, H. Chen, Z. Meng, L. Liu, Z. Xia, J. Sinova, T. Jungwirth, and Z. Liu, An anomalous hall effect in altermagnetic ruthenium dioxide, *Nat. Electron.* **5**, 735 (2022).
- [32] R. D. Gonzalez Betancourt, J. Zubáč, R. Gonzalez-Hernandez, K. Geishendorf, Z. Šobáň, G. Springholz, K. Olejník, L. Šmejkal, J. Sinova, T. Jungwirth, S. T. B. Goennenwein, A. Thomas, H. Reichlová, J. Železný, and D. Kriegner, Spontaneous Anomalous Hall Effect Arising from an Unconventional Compensated Magnetic Phase in a Semiconductor, *Phys. Rev. Lett.* **130**, 036702 (2023).
- [33] X.-Y. Hou, H.-C. Yang, Z.-X. Liu, P.-J. Guo, and Z.-Y. Lu, Large intrinsic anomalous Hall effect in both Nb₂FeB₂ and Ta₂FeB₂ with collinear antiferromagnetism, *Phys. Rev. B* **107**, L161109 (2023).
- [34] X. Zhou, W. Feng, X. Yang, G.-Y. Guo, and Y. Yao, Crystal chirality magneto-optical effects in collinear antiferromagnets, *Phys. Rev. B* **104**, 024401 (2021).
- [35] X. Zhou, W. Feng, R.-W. Zhang, L. Šmejkal, J. Sinova, Y. Mokrousov, and Y. Yao, Crystal Thermal Transport in Altermagnetic RuO₂, *Phys. Rev. Lett.* **132**, 056701 (2024).
- [36] P.-J. Guo, Z.-X. Liu, and Z.-Y. Lu, Quantum anomalous hall effect in collinear antiferromagnetism, *npj Comput. Mater.* **9**, 70 (2023).
- [37] Y.-X. Li, Y. Liu, and C.-C. Liu, Creation and manipulation of higher-order topological states by altermagnets, *Phys. Rev. B* **109**, L201109 (2024).
- [38] P.-J. Guo, Y. Gu, Z.-F. Gao, and Z.-Y. Lu, Altermagnetic ferroelectric LiFe₂F₆ and spin-triplet excitonic insulator phase (2023), [arXiv:2312.13911](https://arxiv.org/abs/2312.13911) [cond-mat.mtrl-sci].
- [39] S. Qu, Z.-F. Gao, H. Sun, K. Liu, P.-J. Guo, and Z.-Y. Lu, Extremely strong spin-orbit coupling effect in light element altermagnetic materials (2024), [arXiv:2401.11065](https://arxiv.org/abs/2401.11065) [cond-mat.mtrl-sci].
- [40] Z.-F. Gao, S. Qu, B. Zeng, Y. Liu, J.-R. Wen, H. Sun, P.-J. Guo, and Z.-Y. Lu, AI-accelerated Discovery of Altermagnetic Materials (2023), [arXiv:2311.04418](https://arxiv.org/abs/2311.04418) [cond-mat.mes-hall].
- [41] Z. Xiao, J. Zhao, Y. Li, R. Shindou, and Z.-D. Song, Spin Space Groups: Full Classification and Applications (2024), [arXiv:2307.10364](https://arxiv.org/abs/2307.10364) [cond-mat.mes-hall].
- [42] S. Zeng and Y.-J. Zhao, The description of two-dimensional altermagnetism (2024), [arXiv:2405.03557](https://arxiv.org/abs/2405.03557).
- [43] Y. Liu, J. Yu, and C.-C. Liu, Twisted Magnetic Van der Waals Bilayers: An Ideal Platform for Altermagnetism (2024), [arXiv:2404.17146](https://arxiv.org/abs/2404.17146) [cond-mat.mtrl-sci].
- [44] J. Krempaský, L. Šmejkal, S. W. D'Souza, M. Hajlaoui, G. Springholz, K. Uhlířová, F. Alarab, P. C. Constantinou, V. Strocov, D. Usanov, W. R. Pudelko, R. González-Hernández, A. B. Hellenes, Z. Jansa, H. Reichlová, Z. Šobáň, R. D. G. Betancourt, P. Wadley, J. Sinova, D. Kriegner, J. Minár, J. H. Dil, and T. Jungwirth, Altermagnetic lifting of Kramers spin degeneracy, *Nature* **626**, 517 (2024).
- [45] T. Osumi, S. Souma, T. Aoyama, K. Yamauchi, A. Honma, K. Nakayama, T. Takahashi, K. Ohgushi, and T. Sato, Observation of a giant band splitting in altermagnetic MnTe, *Phys. Rev. B* **109**, 115102 (2024).
- [46] S. Reimers, L. Odenbreit, L. Šmejkal, V. N. Strocov, P. Constantinou, A. B. Hellenes, R. J. Ubierno, W. H. Campos, V. K. Bharadwaj, A. Chakraborty, T. Deneulin, W. Shi, R. E. Dunin-Borkowski, S. Das, M. Kläui, J. Sinova, and M. Jourdan, Direct observation of altermagnetic band splitting in CrSb thin films, *Nat. Commun.* **15**, 2116 (2024).
- [47] O. Fedchenko, J. Minár, A. Akashdeep, S. W. D'Souza, D. Vasilyev, O. Tkach, L. Odenbreit, Q. Nguyen, D. Kutnyakhov, N. Wind, L. Wenthaus, M. Scholz, K. Rossnagel, M. Hoesch, M. Aeschlimann, B. Stadtmüller, M. Kläui, G. Schönhense, T. Jungwirth, A. B. Hellenes, G. Jakob, L. *checkomejkal*, J. Sinova, and H.-J. Elmers, Observation of time-reversal symmetry breaking in the band structure of altermagnetic RuO₂, *Sci. Adv.* **10**, eadj4883 (2024).
- [48] See Supplemental Material at **, which includes supplemental figures and tables, details of calculation methods and Refs. [63–68].
- [49] E. A. Pruss, B. S. Snyder, and A. M. Stacy, A New Layered Ternary Sulfide: Formation of Cu₂WS₄ by Reaction of WS₄²⁻ and Cu⁺ Ions, *Angew. Chem. Int. Ed. Engl.* **32**, 256 (1993).
- [50] C. J. Crossland, P. J. Hickey, and J. S. O. Evans, The synthesis and characterisation of Cu₂MX₄ (M = W or Mo; X = S, Se or S/Se) materials prepared by a solvothermal method, *J. Mater. Chem.* **15**, 3452 (2005).
- [51] P. D. Tran, M. Nguyen, S. S. Pramana, A. Bhattacharjee, S. Y. Chiam, J. Fize, M. J. Field, V. Artero, L. H. Wong, J. Loo, and J. Barber, Copper molybdenum sulfide: a new efficient electrocatalyst for hydrogen production from water, *Energy Environ. Sci.* **5**, 8912 (2012).
- [52] Y. Lin, S. Chen, K. Zhang, and L. Song, Recent Advances of Ternary Layered Cu₂MX₄ (M = Mo, W; X = S, Se) Nanomaterials for Photocatalysis, *Solar RRL* **3**, 1800320 (2019).
- [53] R. Balu, S. K. Sundaram, S. Rameshkumar, K. Aravinth, and P. Ramasamy, Controlled growth of 2D structured Cu₂WS₄ nanoflakes for high-performance all-solid-state supercapacitors, *J. Electroanal. Chem.* **922**, 116718 (2022).
- [54] F. Zhan, Q. Wang, Y. Li, X. Bo, Q. Wang, F. Gao, and C. Zhao, Low-Temperature Synthesis of Cuboid Silver Tetrathiotungstate (Ag₂WS₄) as Electrocatalyst for Hydrogen Evolution Reaction, *Inorg. Chem.* **57**, 5791 (2018).
- [55] D. Xiao, M.-C. Chang, and Q. Niu, Berry phase effects on electronic properties, *Rev. Mod. Phys.* **82**, 1959 (2010).
- [56] K. F. Mak, K. L. McGill, J. Park, and P. L. McEuen, The valley Hall effect in MoS₂ transistors, *Science* **344**, 1489 (2014).

- [57] D. Xiao, G.-B. Liu, W. Feng, X. Xu, and W. Yao, Coupled Spin and Valley Physics in Monolayers of MoS₂ and Other Group-VI Dichalcogenides, *Phys. Rev. Lett.* **108**, 196802 (2012).
- [58] E. C. Marino, L. O. Nascimento, V. S. Alves, and C. M. Smith, Interaction Induced Quantum Valley Hall Effect in Graphene, *Phys. Rev. X* **5**, 011040 (2015).
- [59] A. Subedi, L. Zhang, D. J. Singh, and M. H. Du, Density functional study of FeS, FeSe, and FeTe: Electronic structure, magnetism, phonons, and superconductivity, *Phys. Rev. B* **78**, 134514 (2008).
- [60] H.-Y. Cao, S. Chen, H. Xiang, and X.-G. Gong, Antiferromagnetic ground state with pair-checkerboard order in FeSe, *Phys. Rev. B* **91**, 020504 (2015).
- [61] K. Liu, Z.-Y. Lu, and T. Xiang, Nematic antiferromagnetic states in bulk FeSe, *Phys. Rev. B* **93**, 205154 (2016).
- [62] Q. Wang, Y. Shen, B. Pan, X. Zhang, K. Ikeuchi, K. Iida, A. D. Christianson, H. C. Walker, D. T. Adroja, M. Abdel-Hafez, X. Chen, D. A. Chareev, A. N. Vasiliev, and J. Zhao, Magnetic ground state of FeSe, *Nat. Commun.* **7**, 12182 (2016).
- [63] P. E. Blöchl, Projector augmented-wave method, *Phys. Rev. B* **50**, 17953 (1994).
- [64] G. Kresse and J. Furthmüller, Efficiency of ab-initio total energy calculations for metals and semiconductors using a plane-wave basis set, *Comput. Mater. Sci.* **6**, 15 (1996).
- [65] J. P. Perdew, K. Burke, and M. Ernzerhof, Generalized Gradient Approximation Made Simple, *Phys. Rev. Lett.* **77**, 3865 (1996).
- [66] A. A. Mostofi, J. R. Yates, Y.-S. Lee, I. Souza, D. Vanderbilt, and N. Marzari, wannier90: A tool for obtaining maximally-localised Wannier functions, *Comput. Phys. Commun.* **178**, 685 (2008).
- [67] Q. Wu, S. Zhang, H.-F. Song, M. Troyer, and A. A. Soluyanov, WannierTools: An open-source software package for novel topological materials, *Comput. Phys. Commun.* **224**, 405 (2018).
- [68] L. Liu, X. Ren, J. Xie, B. Cheng, W. Liu, T. An, H. Qin, and J. Hu, Magnetic switches via electric field in BN nanoribbons, *Appl. Surf. Sci.* **480**, 300 (2019).